



Reveal the role of inert groups in donor-acceptor conjugated polymer for two opposite photocatalytic reactions

Fengxuan Zhang^a, Fanxing Zhou^a, Shiheng Yin^c, Bei Long^a, Guo-Jun Deng^a, Atif Ali^d,
Ting Song^{a,b,*}

^a Key Laboratory for Green Organic Synthesis and Application of Hunan Province, Key Laboratory of Environmentally Friendly Chemistry and Application of Ministry of Education, College of Chemistry, Xiangtan University, Xiangtan 411105, China

^b School of Chemistry and Chemical Engineering, Henan Normal University, Xinxiang 453007, China

^c Analytical and Testing Center, South China University of Technology, Guangzhou 510640 China

^d Department of Chemistry and State Key Laboratory of Synthetic Chemistry, The University of Hong Kong, Pokfulam Road, Hong Kong, China

ARTICLE INFO

Keywords:

D-A structure
Thioether oxidation
CO₂ reduction
High selectivity
Inert group

ABSTRACT

Oxidation and reduction reactions are two distinct reactions, and the efficient driving of these two reactions through a photocatalyst is of great significance in the field of catalysis. In this work, donor-acceptor conjugated polymers with different inert groups were designed and synthesized using cyclotriphosphazene as the electron donor (D) and s-triazine ring as the electron acceptor (A), respectively. The result showed that the introduction of methyl groups preserved the D-A structure in the conjugated polymer (Me-COP). The migration ability of photogenerated carriers and the adsorption of reactant sequences in Me-COP sample were significantly optimized due to their own hyperconjugation and steric hindrance. Under visible light irradiation, Me-COP exhibited good selective reduction activity of CO₂ to CH₄. Me-COP for thioether oxidation to sulfoxide also showed excellent selective photocatalytic activity. This study underlines the significance of adding inert groups to the conjugated polymers in order to create multifunctional photocatalysts.

1. Introduction

Photocatalytic reduction of CO₂ to hydrocarbon fuels is a promising way to mitigate global warming and energy scarcity. [1–3] Unfortunately, the high dissociation energy of the C=O bond (750 KJ mol⁻¹) poses a significant thermodynamic barrier to the activation and reduction of CO₂. [4,5] Thioether oxidation is the simplest and most often used process for creating sulfoxide, which can be used to produce a number of chemically and therapeutically active compounds. [6,7] It has been extensively researched to substitute the conventional thermal oxidation synthesis technique with the photocatalytic oxidation of thioethers using O₂, which has the advantages of a straightforward process, environmental friendliness, and moderate reaction conditions (e.g. room temperature and atmospheric pressure). [8–10] Within past years, selective benzylamine oxidation and proton photoreduction on photocatalysts can be performed simultaneously in a single oxidation-reduction cycle to yield two value-added products of solar fuel and solar chemicals. [11] However, such reactions are mostly found in

photocatalytic hydrogen production, and the organic reactions that can be applied are significantly limited. [12–15] Thus, the use of multifunctional photocatalysts that can drive two different reactions remains a serious challenge.

Polymer photocatalysts have received much attention because of their low cost, low toxicity, adjustable backbone structure and suitable band gap. [16–18] However, most polymer catalysts generally suffer from low photoinduced electron transfer and poor CO₂ absorption capacity, resulting in low efficiency. [19] In recent years, phosphonitrile-based polymers have gradually attracted the attention of researchers because of their P = N covalent bonding and stable conjugated ring structure. [20–23] When P and N are bonded, the outer electrons of P are shifted as a whole, which shows that the electrons around it are strongly off-domain. [24–26] A large number of off-domain electrons can interact with the guest molecules (such as CO₂ and reaction intermediates) via Lewis acid-base reactions. [27,28] In addition to preventing photogenerated charge recombination, the electron-absorbing s-triazine unit acts as a typical electron acceptor,

* Corresponding author at: Key Laboratory for Green Organic Synthesis and Application of Hunan Province, Key Laboratory of Environmentally Friendly Chemistry and Application of Ministry of Education, College of Chemistry, Xiangtan University, Xiangtan 411105, China.

E-mail address: songtg@xtu.edu.cn (T. Song).

<https://doi.org/10.1016/j.apcatb.2023.123004>

Received 29 March 2023; Received in revised form 27 May 2023; Accepted 14 June 2023

Available online 16 June 2023

0926-3373/© 2023 Elsevier B.V. All rights reserved.

offering remarkable heteroatomic effects and active sites.[29] A donor-acceptor conjugated polymer is constructed by linking cyclo-triphosphazene to the s-triazine unit via an imine group. Whereas both the s-triazine structure and cyclo-triphosphazene can act as Lewis bases for CO₂ adsorption, the rapid migration of photoinduced electrons is significantly inhibited by the limited electron density of the imine bond itself, which cannot establish an effective electron channel.[30].

In order to modulate the migration and transport of photogenerated carriers, the introduction of inert groups in the D-A polymers is one of the very effective strategies. The attachment of different inert groups (-F, N-alkyl, -OCH₃, etc.) can improve the distribution of off-domain electrons on the catalyst's backbone, as well as to accelerate the transport efficiency of photoinduced electron.[31,32] Voort et al. describe that chlorine and fluorine atoms favor the π -electron delocalization of conjugated polymers and can modulate their electronic structure, leading to a significant enhancement of photocatalytic performance. [33] Logan et al. reported that through the introduction of N-alkyl groups in the organic linkage of 2-aminoterephthalate, the MIL-125-NH₂ catalysts exhibited a tunable band gap and accelerated photogenerated carrier migration, presenting excellent photocatalytic activity. [34] Therefore, with the help of its own potential conjugated structure and steric hindrance, some inert groups can control the carrier migration and the reactant adsorption capacity in the D-A polymer, thus achieving two completely different types of reactions, which have not been reported yet.

In this study, several inert groups (methyl, phenyl) were embedded in the framework of donor (D)-acceptor (A) conjugated polymer. This push-pull mechanism promotes photoinduced carrier separation and associated charge migration to the catalyst surface or substrate, resulting in effective catalytic activity. By utilizing its hyperconjugation and steric hindrance, the methyl group in the D-A conjugated polymer (Me-COP) improves the directional electron migration and reactive adsorption sequence, according to calculations based on density-driven theory (DFT) and experimental findings. The methyl group in Me-COP not only significantly enhanced the activity and selectivity of the photocatalytic reduction of CO₂ to CH₄ compared with the inert group-free and phenyl group, but also displayed good efficacy in the selective oxidation of thioethers to sulfoxide using photocatalysis. In this work, the concept of introducing suitable inert groups into the D-A conjugated polymer was proposed for the fabrication of high-performance multifunctional photocatalysts.

2. Experimental section

2.1. Synthesis of photocatalysts

2,4-diamino-6-methyl-1,3,5-triazine (3 mmol) and hexachlorocyclotriphosphazene (2 mmol) were dissolved in 24 mL CH₃CN and 6 mL DMSO mixed solution to form a clear solution. The transparent solution was put into a 50 mL hydrothermal reactor and heated for 24 h at 180 °C. The clear solution was suitably centrifuged after cooling to ambient temperature, rinsed to remove CH₃CN and DMSO, and the dark red powder was isolated and dried to obtain the Me-COP sample. For comparison, two control samples were also prepared. COP and Ph-COP samples were obtained under the same conditions except that 2,4-diamino-6-phenyl-1,3,5-triazine and 2,4-diamino-1,3,5-triazine were used instead of 2,4-diamino-6-methyl-1,3,5-triazine, respectively.

2.2. Material characterization

X-ray diffraction (XRD) patterns were conducted by an X-ray diffractometer (D8 ADVANCE, Bruker) to investigate the crystal phase structures of samples. Fourier transform infrared (FT-IR, Nicolet iS 50, Thermo Scientific) spectra with an attenuated total reflectance (ATR) mode, and X-ray photoelectron spectra (XPS, Escalab 250xi, Thermo Scientific) were implemented to determine the chemical structure of

samples. UV-vis diffuse reflectance spectra (DRS) were obtained by an UV-vis spectrophotometer (UV-2600, Shimadzu) to characterize the light-harvesting capacity of samples. BaSO₄ was used as the reflectance standard. Transmission electron microscopy (TEM, Titan G2 60-300, FEI) was carried out to observe the microstructure of photocatalysts, and corresponding energy dispersive X-ray spectroscopy-element mapping (EDS-Mapping) was collected to observe the element distribution. Nitrogen adsorption-desorption isotherms were recorded by nitrogen adsorption apparatus (ASAP2020, Micromeritics) to obtain the specific surface area of materials. Electron spin resonance (ESR, MEX-nano, Bruker) was conducted to analyze the intermediates of photocatalytic reaction. Atomic force microscopy (AFM) was conducted to measure the thickness of samples. To investigate the migration and separation efficiency of photoinduced carrier, steady-state photoluminescence (PL, F-7000, Hitachi) and time-resolved photoluminescence (TRPL, FLS-1000, Edinburgh) spectra were obtained.

2.3. Photocatalytic CO₂ reduction

In order to prevent photothermal effects, photocatalytic CO₂ reduction was done in a quartz reactor with a flowing water filter. In 6 mL of the combined solution (2 mL H₂O, 1 mL TEOA, 3 mL CH₃CN), 5 mg of catalyst was disseminated. The reactor is evacuated and injected with high purity CO₂, and the procedure is repeated three times. As a simulated visible light source, a 300 W xenon lamp (PLS-SXE300UV, Beijing Perfect light) was employed with a 420 nm cut-off filter, and the light was kept on for 6 h. A gas chromatograph (GC7900, Shanghai Tianmei) outfitted with a flame ionization detector (FID) for CO and CH₄ monitoring and a thermal conductivity detector (TCD) for H₂ detection was used to test the generated products.

2.4. Typical procedure for photocatalytic oxidation reaction

The photocatalyst (2 mg), CH₃CH₂OH (2.0 mL), and substrate (0.1 mmol) were all added to a 10-mL quartz tube. A 45 W 420 nm LED lamp was used to illuminate the reaction mixture, and an electric fan was used to cool it such that it remained at room temperature. The mixture was centrifuged to remove any remaining contaminants after the reaction had been going on for 12 h, and the GC/GC-Mass was used to analyse the supernatant.

2.5. Photo-electrochemical measurements

Photocurrent response tests were performed using a DH7000C workstation (Jiangsu Donghua Analytical Instruments Co. Ltd.) with a three-electrode system in 0.1 M Na₂SO₄ solution. A 300 W Xenon lamp (PLS-SXE300UV, Beijing Perfect light) was used as light source. The reference and counter electrodes are silver/silver chloride electrode and platinum sheet, respectively. The working electrode was prepared as follows: 5 mg catalyst was dispersed in a mixed solution containing 1 mL methanol. Then, the suspension was dropped onto the surface of an ITO plate with an area of 1.0 × 1.0 cm². The working electrodes were dried, and the photo-responsive signals of the samples were measured under alternating light on and off. Electrochemical impedance spectroscopy (EIS) was measured on a same instrument in a standard three-electrode system with a bias potential of -0.2 V and a frequency range from 1 to 10⁵ Hz. Mott-Schottky tests were performed on a same instrument in a standard three-electrode system at different frequencies (500 Hz, 1000 Hz).

3. Results and discussion

3.1. Composition and structure

A D-A conjugated polymer is prepared by connecting s-triazine and cyclo-triphosphazene through the imine bond (Fig. 1). In addition,

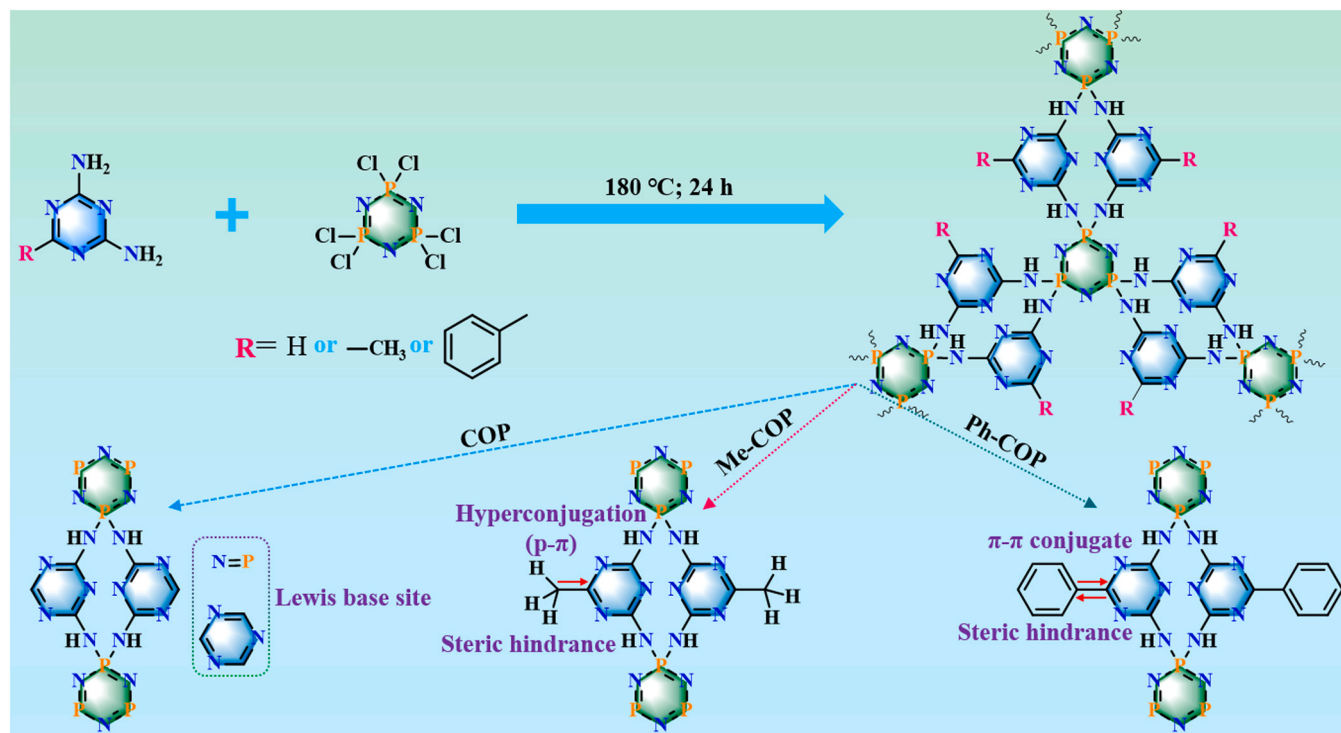


Fig. 1. Synthesis of COP, Me-COP and Ph-COP samples.

different inert functional groups (methyl and phenyl) were introduced on s-triazine ring to control the photogenerated carrier migration and the order of adsorption sites of the whole polymer. The existence of methyl in Me-COP samples was proved by the characteristic peak of methyl at 1450 cm⁻¹ in Fourier transform infrared (FT-IR) spectroscopy. The characteristic peak at 730 cm⁻¹ indicates the presence of benzene ring in Ph-COP sample. In addition, the peak at about 1200 cm⁻¹ in the all samples proved the existence of the P = N bond of

cyclotriphosphazene, the peak at 1635 cm⁻¹ belonged to the C-N bond in COP, Me-COP and Ph-COP samples, and the peak at 2800–3600 cm⁻¹ showed that the amine group in the three samples reacted with cyclo-triphosphazene (Fig. 2a). P-Cl did not exhibit its typical absorption at 601 cm⁻¹, demonstrating that the chlorine atoms were virtually entirely replaced. [35] Further testing of the chlorine content showed that all samples contained only very low levels of chlorine (Table S1). The characteristic signal peak, which corresponds to the carbon atom on the

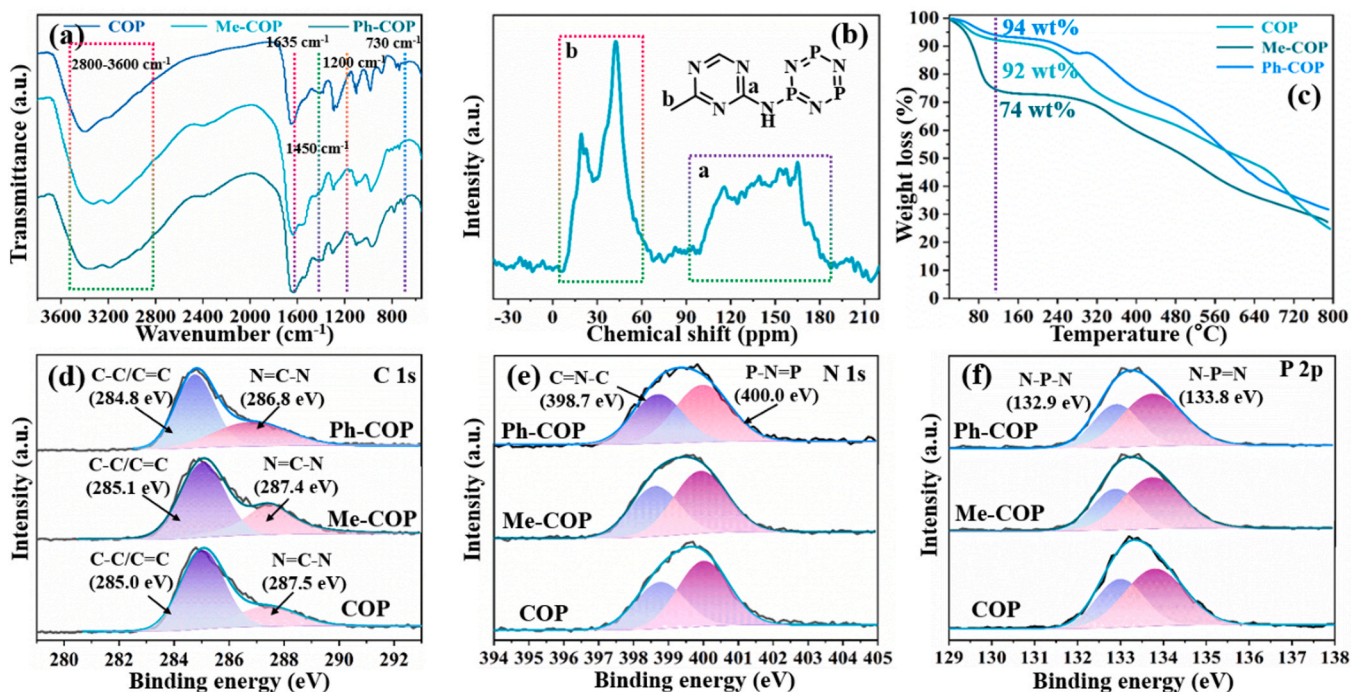


Fig. 2. (a) FT-IR spectra of COP, Me-COP and Ph-COP samples. (b) Solid-state ¹³C NMR spectrum of Me-COP. (c) Thermogravimetric analysis results of COP, Me-COP and Ph-COP samples. XPS spectra of COP, Me-COP and Ph-COP samples: (d) C 1s, (e) N 1s, and (f) P 2p.

methyl group, was visible at around 19–42 ppm in the solid-state ^{13}C NMR spectra of Me-COP polymer. The carbon atom on the s-triazine ring can be attributed to the peak at 114–166 ppm (Fig. 2b). [36–38] The aforementioned findings offer preliminary confirmation of the creation of polymers with the D-A structure. The three polymers display weak and wide diffraction peaks in powder X-ray diffraction (XRD) patterns, indicating their amorphous characteristics (Fig. S1). The thermogravimetric analysis showed that the mass loss in Me-COP was more than 26 wt% compared with COP and Ph-COP. The results showed that methyl group was very easy to break bonds and overflow from the skeleton at 120 °C in air atmosphere (Fig. 2c). Interestingly, the residual quality of the three samples at 790 °C is not significantly different due to the same main chemical framework. Similar surface areas are found in all polymers ($4.01\text{ m}^2\text{ g}^{-1}$ for COP, $6.13\text{ m}^2\text{ g}^{-1}$ for Ph-COP, $12.21\text{ m}^2\text{ g}^{-1}$ for Me-COP), which may be a result of their similar topologic structures (Fig. S2).

These samples' chemical environments for C, N, and P atoms were further examined by XPS characterization. The graphitic carbon (C-C/C=C) and N = C-N construction are respectively associated with the subpeaks of 285.0 eV and 287.5 eV deconvoluted from COP's C 1s spectrum (Fig. 2d). Because the C-C bond from the methyl group and the C=C bond on the benzene ring overlap with the graphite carbon in the Me-COP and Ph-COP sample, it cannot be clearly distinguished. However, compared with COP, the C 1s peak of Ph-COP has a blue shift as a whole, while that of Me-COP has the same binding energy. This may be because the π - π conjugation on the benzene ring disperses the electron

distribution in Ph-COP sample. With binding energies of 398.7 and 400.0 eV, the C=N-C fragment in the s-triazine heterocycle and the P = N-P fragment in cyclotriphosphazene are the sources of two N 1s subpeaks present in all samples, respectively (Fig. 2e). [30] For the P 2p spectra, 132.9 eV and 133.8 eV peaks fitted in all samples origin from N-P-N and N-P = N, respectively (Fig. 2f). [38] All of the aforementioned findings suggest that D-A conjugated polymers with various inert groups were successfully produced.

The external morphology of Me-COP is investigated by TEM and HRTEM. Me-COP shows ultrathin lamellar structure (Figs. 3a and 3b). HRTEM tests find that it is an amorphous structure (Fig. 3c). Further amplification can probe that the irregular ring and the regular ring are adjacent to each other in Me-COP sample (Fig. 3d). According to atomic force microscopy, there are many mountain-like overlaps on the surface of Me-COP (Fig. 3e). This may be due to the introduction of methyl groups, as they extend in different directions. The thickness of Me-COP is approximate 5 nm, suggesting an ultrathin structure for Me-COP (Fig. S3). Also, the elemental mapping analysis reveals that N, C, and P are distributed uniformly throughout Me-COP (Fig. 3f-o). UV-Vis DRS spectroscopy to visualize the optical absorption properties of COP, Me-COP and Ph-COP. Due to their substantial conjugated backbones, all samples exhibit broad and potent visible-light absorption in the 400–800 nm region as seen in Fig. S4. Notably, the light absorption intensity of Me-COP is better than that of COP and Ph-COP, because the hyperconjugation of methyl group increases the delocalized electron density on the polymer skeleton. Correspondingly, the apparent color of

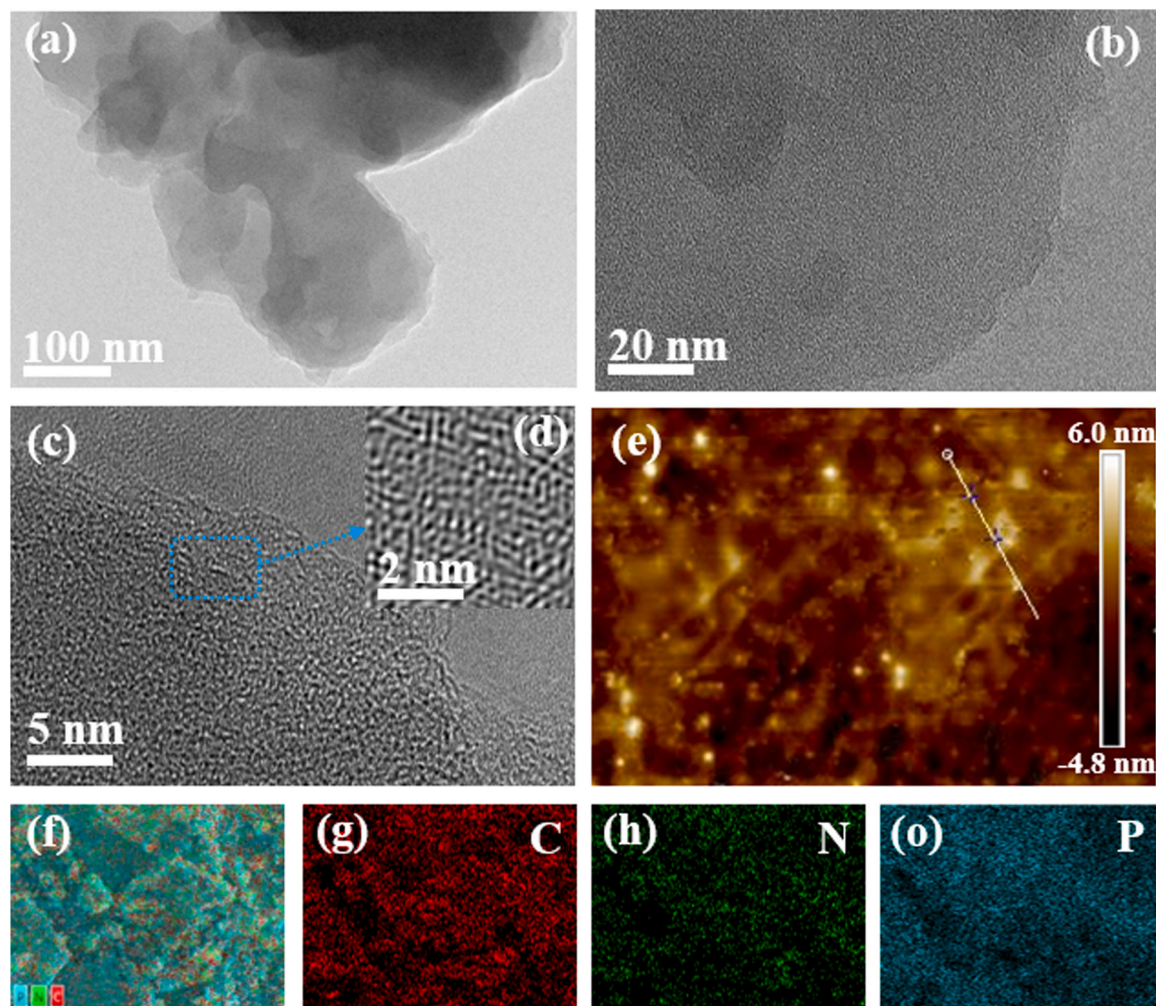


Fig. 3. TEM images (a, b) of Me-COP. HRTEM images (c, d) of Me-COP. AFM image (e) of Me-COP. Elemental mappings (f-o) of Me-COP.

Me-COP sample is also significantly darker than that of COP and Ph-COP as seen in Fig. S5. According to the Tauc plots, the optical bandgaps (E_g) of COP, Me-COP, and Ph-COP are 1.71, 1.64 and 1.68 eV, respectively (Fig. S6). As shown in Fig. S7, the Mott-Schottky plot has a positive slope, which confirms that COP, Me-COP, and Ph-COP are all n-type semiconductors, and the conduction band (CB) of the n-type semiconductor is usually 0.1 eV negative than its flat-band position. [39] Therefore, CB energies for COP, Me-COP, and Ph-COP are determined to be -0.68 , -0.92 , and -0.69 V, respectively. As a result, the valence-band (VB) locations of COP, Me-COP, and Ph-COP are 1.03, 0.72, and 0.99 V relative NHE, respectively. Fig. S8 displays the relevant energy level diagram. Therefore, constructing the D-A conjugated polymer with methyl group optimizes the band structure, making it more suitable for the redox reaction.

3.2. Photocatalytic CO_2 reduction performance

The performance of COP, Me-COP, and Ph-COP samples in photocatalytic CO_2 reduction under visible light was tested in a CO_2 (1.0 atm, 298 K) atmosphere devoid of photosensitizers and co-catalysts. Without H_2 products, CO and CH_4 were found to be the primary reduction products for all examined catalysts. With the passage of reaction time, the fast to slightly slow increase in CH_4 yield for all samples may be due to the occupation of part of the active site by the progressively increasing CO and CH_4 products, which is similar to the phenomenon reported in other literature (Fig. 4a). [40,41] As shown in Fig. 4b, the product activity (CH_4 : $861.3 \mu\text{mol g}^{-1}$; CO: $52.7 \mu\text{mol g}^{-1}$) of Me-COP sample is significantly higher than that of Ph-COP sample (CH_4 : $550.6 \mu\text{mol g}^{-1}$; CO: $61.9 \mu\text{mol g}^{-1}$), especially that of COP sample (CH_4 : $33.0 \mu\text{mol g}^{-1}$; CO: $22.6 \mu\text{mol g}^{-1}$). It can also be seen that the CH_4 selectivity of Me-COP sample (94.2%) is much higher than that of COP (59.4%) and Ph-COP (89.9%). Under the same conditions, we compared the synthesis of Me-COP with that of monomer 1, monomer 2, and Me-COP. The outcomes showed that before these two monomers may be used for CO_2 reduction, they must first be combined into a conjugated polymer

(Fig. S9). We conducted control experiments and found that no gas products were detected, indicating that the carbon source of CH_4 and CO was from CO_2 molecules (Fig. 4c). The exceptional photostability of Me-COP is also demonstrated by the performances of Me-COP, which has not significantly decline after four consecutive runs with each run lasting six hours (Fig. 4d). XRD and FT-IR spectra of Me-COP after the stability tests, which further supported by the skeleton structure (Fig. S10 and 11). The original gas data of Me-COP further proved that CH_4 was the main component of gas product, and its selectivity was up to 94.2% (Fig. 4e). Moreover, $^{13}\text{CO}_2$ was used as a reactant in the isotope labeling experiment to identify the carbon source. As shown in Fig. S12 and Fig. 4f, the characteristic signals of ^{13}CO and $^{13}\text{CH}_4$ were observed at $m/z = 13$, 16, 29 and $m/z = 13$, 14, 15, 16, 17, respectively, which confirmed that the carbon source of the reduction reaction was CO_2 . All of these findings suggest that Me-COP has the ability to effectively and selectively photoreduce CO_2 to CH_4 . It is important to note that Me-COP's efficiency at reducing CO_2 exceeds that of sophisticated photocatalysts (Table S2).

3.3. Photocatalytic selective oxidation of thioethers

Initial testing of Me-COP's photocatalytic activity used the oxidation of thioanisole as a model reaction (Table 1). Me-COP successfully catalyzed the conversion of thioanisole under 420 nm irradiation with O_2 as the oxidant, and after 12 h of reaction, the yield of (methylsulfinyl)benzene was about 100% (Table 1, Entry 3). Several controlled studies were carried out to better understand the variables influencing the oxidation process of thioanisole. As no product was found in the dark environment, it is likely that visible light was used to fuel the oxidation reaction (Table 1, Entry 1). The yield of (methylsulfinyl)benzene was only 9.5% in the absence of Me-COP, further demonstrating its efficient photocatalytic activity in this chemical system (Table 1, Entry 2). However, the yield of (methylsulfinyl)benzene in the air reduced to 18% and the reaction was difficult to carry out in a N_2 environment, suggesting that O_2 was crucial to the reaction's success (Table 1, Entry 4 and

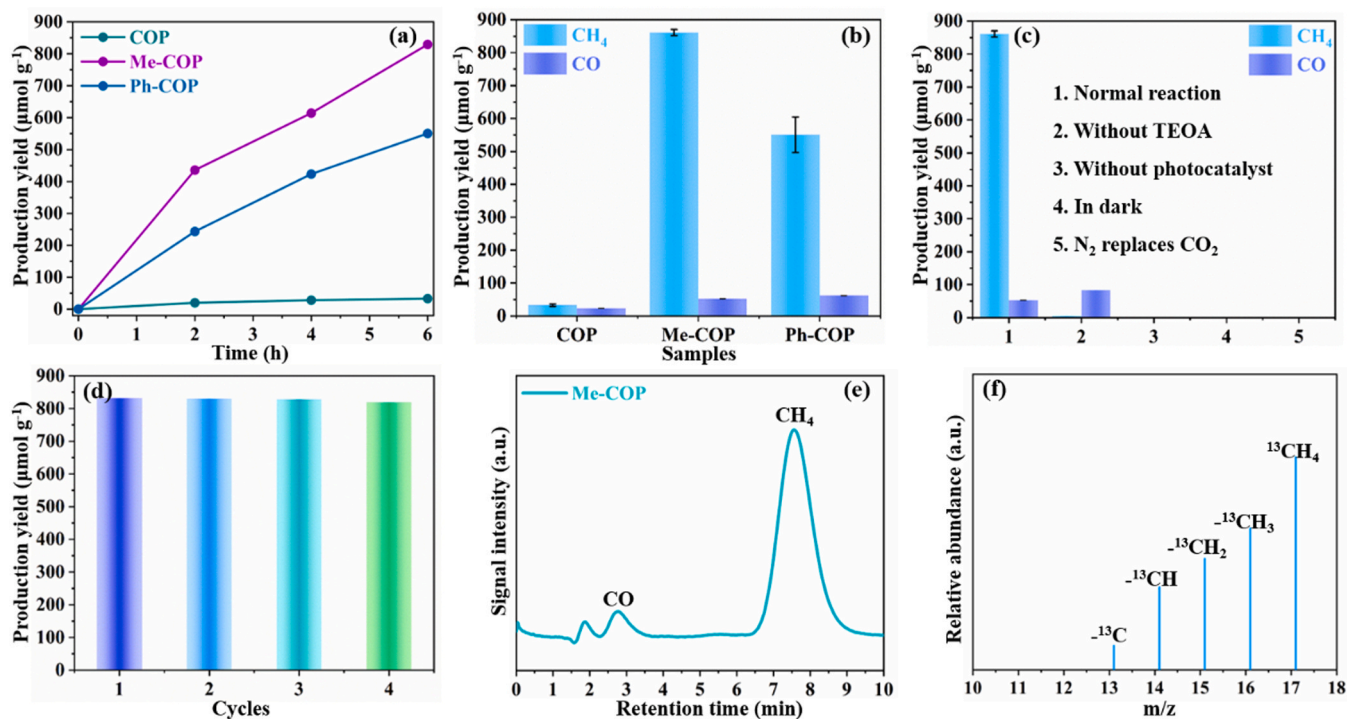
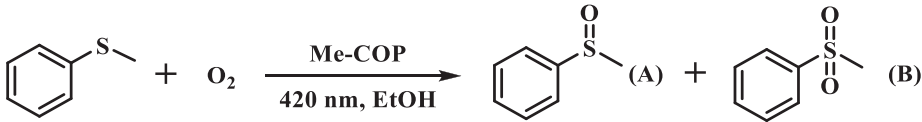


Fig. 4. (a) Photocatalytic CO_2 cumulative curve for CH_4 over COP, Me-COP and Ph-COP samples. (b) Photocatalytic CO_2 production yield for COP, Me-COP and Ph-COP samples. (c) Control experiments of Me-COP sample. (d) Cycling stability test (6 h per cycle). (e) GC spectrum of Me-COP. (f) GC-MS analysis of Me-COP by using $^{13}\text{CO}_2$ as reactant.

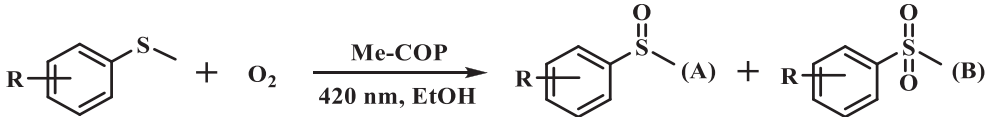
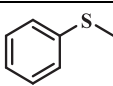
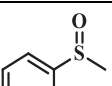
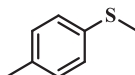
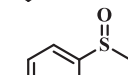
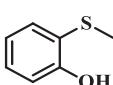
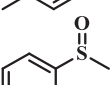
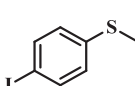
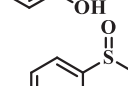
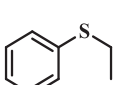
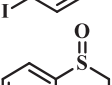
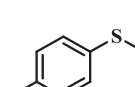
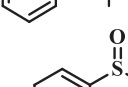
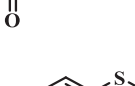
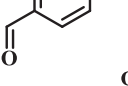
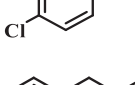
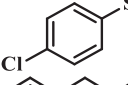
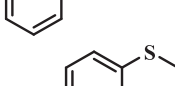
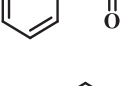
Table 1
Optimization of reaction conditions in the photocatalytic selective oxidation of thioanisole.

			
Entry	Variation from standard conditions	Conversion [%] (A+B)	Selection [%] (A)
1	No light	0	0
2	No catalyst	< 9.5	0
3	O ₂	100	100
4	Air	18	100
5	N ₂	0	0

Reaction conditions: 0.1 MPa O₂, substrate (0.1 mmol), catalyst, LED irradiation for 12 h at room temperature. Product formation (yield) obtained by GC/FID.

- 5). To speculate on the reaction process, it is essential to identify reactive oxygen species. Quenching tests were used to confirm the reactive oxygen species required for the particular production of (methylsulfinyl) benzene with O₂ over Me-COP sample. The different types of radicals are identified by adding the corresponding radical trapping agents, and there are just two main types of radicals that react with oxygen (¹O₂, O₂^{•−}). When 2,2,6,6-tetramethylpiperidine oxide (TEMPO) is used, its

Table 2
Substrate scope of photocatalytic selective oxidation of thioethers.

				
Entry	Substrate	Product	Conversion [%] (A+B)	Selection [%] (A)
1			100	100
2			100	91.6
3			100	100
4			96.6	95.2
5			92.3	96.4
6			77.5	96.9
7			78.5	93.6
8			93.1	75.1
9			69.1	100

Reaction conditions: 0.1 MPa O₂, substrate (0.1 mmol), catalyst, LED irradiation for 12 h at room temperature. Product formation (yield) obtained by GC/FID.

activity is clearly inhibited, indicating that it is a $^1\text{O}_2$ radical that is involved in the reaction (Table S3, Entry 1). [42] Furthermore, different levels of oxidation occurred throughout (methylsulfinyl)benzene conversions, indicating the presence of $^1\text{O}_2$ as the reaction developed. What's more, the longer electron-hole pair separation caused the reaction to be hindered when one equivalent of AgNO_3 and KI were added to the reaction system as an electron scavenger and hole trapping agent, respectively (Table S3, Entry 3 and 4). [43,44] In order to gain insight into the free radical species, ESR spectra were also used. Under lighting, Me-COP could clearly detect singlet oxygen ($^1\text{O}_2$) radicals (Fig. S13). The ESR results may potentially demonstrate that $^1\text{O}_2$ is involved in the selective oxidation of thioethers by photocatalysis. [45,46] Several aromatic thioethers were exposed to aerobic oxidation in the presence of Me-COP to test the general application of Me-COP (Table 2 and Fig. S14-22). In the presence of Me-COP catalyst, all thioethers are mainly converted to corresponding sulfoxide and the content of sulphone is very low. In contrast to thioanisole derivatives having an electron-releasing group (Me), it is obvious that thioanisole derivatives

with electron-absorbing group ($-\text{CHO}$, $-\text{Cl}$ and $-\text{NO}_2$) have relatively poor activity but little difference in selectivity (Table 2, Entry 6,7 and 9). It is noteworthy that the 2-(methylthio)phenol, which should have low reactivity, is oxidized to the required sulfoxide with 100% high yield and 100% selectivity (Table 2, Entry 3). Ethyl(phenyl)sulfane and benzyl(methyl)sulfane were also effectively converted into (ethylsulfinyl)benzene and ((methylsulfinyl)methyl)-benzene with yields of 92.3% and 93.1%, respectively (Table 2, Entry 5 and 8). Importantly, Me-COP also showed excellent activity of thioether oxidation to sulfoxide comparable to that of metal-based photocatalysts (Table S4).

3.4. Clarification of the proposed mechanism

In order to find out more about the splitting and recombination of photoexcited carrier, photoluminescence (PL) spectra were tested. Me-COP exhibits a noticeably diminished PL peak as opposed to a higher PL peak, which suggests that the chemical structure has been modified to significantly reduce carrier recombination (Fig. 5a). To track the

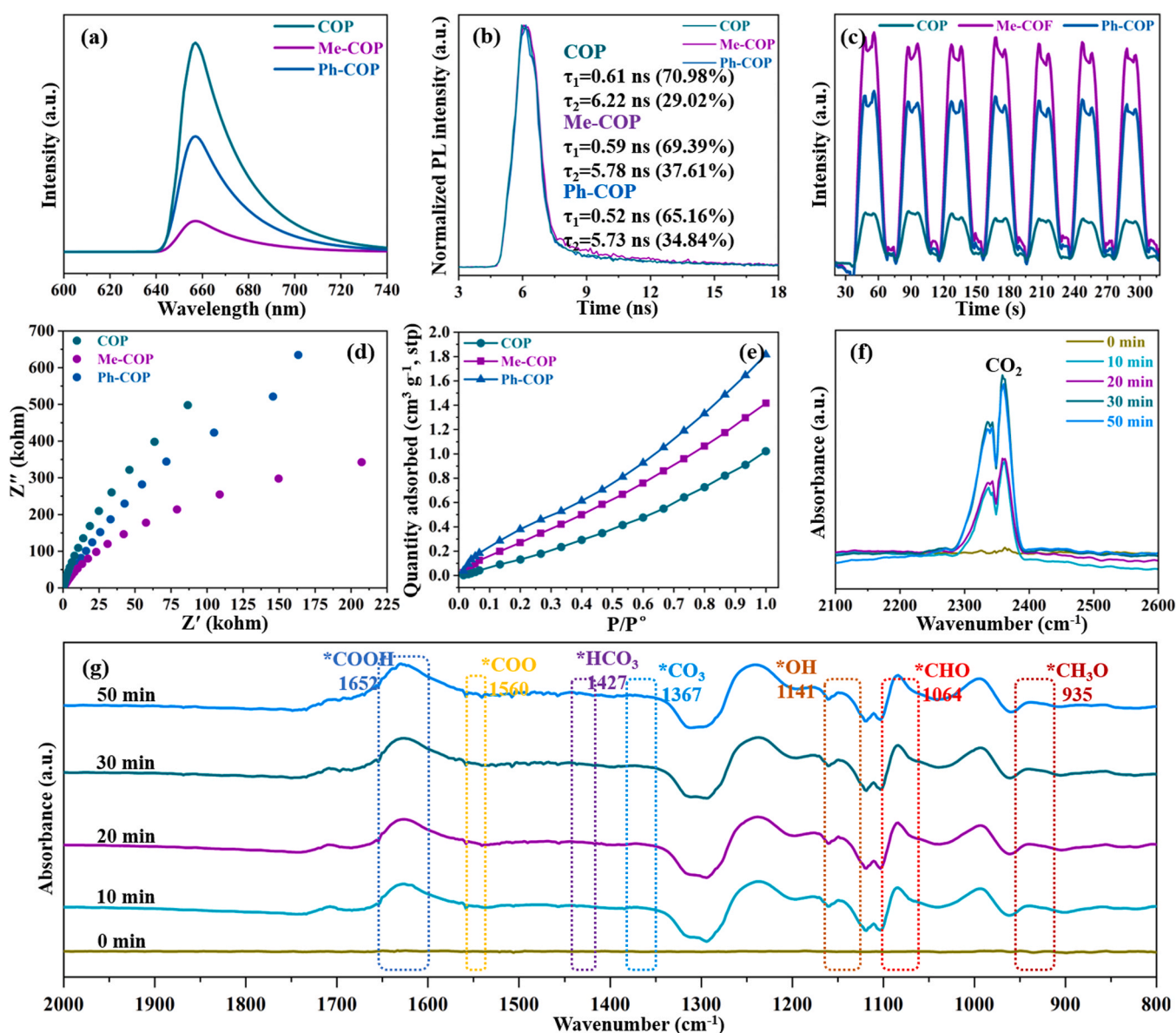


Fig. 5. (a) PL spectra of COP, Me-COP and Ph-COP samples. (b) TRPL spectra of COP, Me-COP and Ph-COP samples. (c) Photocurrents of COP, Me-COP and Ph-COP samples. (d) Electrochemical impedance spectra of COP, Me-COP and Ph-COP samples. (e) CO_2 adsorption-desorption isotherm of COP, Me-COP and Ph-COP samples. (f, g) In-situ FT-IR spectra of Me-COP.

kinetics of electron transport, time-resolved photoluminescence (TRPL) spectra were taken (Fig. 5b). The average fluorescence lifetime of COP, Me-COP, and Ph-COP is 2.24, 2.58, and 2.34 ns, respectively, according to fitting values using the tri-exponential model. Longer Me-COP lifetime suggests more effective photoexcited carrier separation, which is consistent with the smaller Nyquist curve radius from electrochemical impedance spectra (ESI) and the clearly improved transient photocurrent responsiveness (Figs. 5c and 5d). [47] The redox behavior of Me-COP sample and its monomer was investigated by cyclic voltammetry (CV) (Fig. S23 and 24). Monomer 1 showed two large oxidation peaks at 1.02/1.35 V and two consecutive reduction peaks at $-0.62/-0.96$ V and $-1.24/-1.46$ V, indicating that it is also characterized by single-electron oxidation and two-electron reduction. Monomer 2 displays two larger oxidation peaks at 1.03/1.21 V and two consecutive reduction peaks at $-0.60/-0.73$ V and $-1.24/-1.41$ V, indicating that it is also characterized by single-electron oxidation with two-electron reduction. For the Me-COP sample, it shows two peaks at 0.03/0.32 V above the oxidation peak of the monomer and two consecutive peaks at $-0.01/-1.44$ V and -0.32 V above the reduction peak of the monomer, indicating that it inherits the characteristics of one-electron oxidation and two-electron reduction of the monomer. The oxidation ability (loss of electrons) of Me-COP is also enhanced compared to that of the monomer. According to these observations, adding methyl groups to a D-A structure causes a noticeable acceleration in the migration rates of photoinduced carriers.

The CO₂ adsorption capacity of COP, Me-COP and Ph-COP was studied via CO₂-BET measurement (Fig. 5e). After the introduction of methyl and phenyl groups, the maximum capacity of Me-COP and Ph-COP for CO₂ was 1.42 cm³ g⁻¹ and 1.82 cm³ g⁻¹, respectively, which are significantly higher than that of COP sample (1.02 cm³ g⁻¹). The results showed that the introduction of inert groups made the adsorption of CO₂ molecules on the active sites of multiple Lewis acid-bases more orderly, which significantly improved the adsorption capacity of CO₂. The variation of the species during the adsorption, activation, and conversion processes of CO₂ was precisely followed by in-situ FT-IR in order to make a thorough investigation on the mechanism of selective CO₂ photoreduction to CH₄ by building Me-COP. Fig. 5f shows the change of the molecular content of CO₂ adsorbed on Me-COP over time under light conditions. In more detail, the peaks at about 2323–2355 cm⁻¹ are attributed to the asymmetric stretching vibration of adsorbed CO₂ molecules. [48,49] Obviously, with the passage of time, Me-COP represents that the density of these CO₂ molecular peaks first gradually increases and then gradually decreases, indicating that the participation of CO₂ molecules adsorbed on its surface in the reduction reaction is significantly increased. In-situ FT-IR is used to probe the intermediates adsorbed on the surface of Me-COP sample in the photocatalytic CO₂ reduction reaction (Fig. 5g). Absorption peaks corresponding to carbonate were observed at 1427 cm⁻¹ (*HCO₃) and 1367 cm⁻¹ (*CO₃). [50] An important intermediate in the photochemical conversion of CO₂ to CH₄ or CO, *COOH is credited with the peak at 1652 cm⁻¹. More significantly, *CHO, another significant step in the production of CH₄, can be identified by the absorption peak at 1064 cm⁻¹. [51] In addition, the IR peak at 935 cm⁻¹ seems to be a vibration of the *CH₃O group, which is further supported by the reaction that creates CH₄.

In order to further study the effect of inert groups on the charge distribution, the HOMO and LUMO orbital distributions of all samples are derived from DFT calculations (Fig. S25). For COP, HOMO is distributed in the cyclotriphosphazene unit, while LUMO is mainly located in the s-triazine ring, indicating that the conjugated polymer prepared is a typical D-A structure. [52] After the introduction of methyl groups, the electronic distribution of HOMO and LUMO on the skeleton was not significantly affected, and it was still D-A structure. Interestingly, the electron density on the s-triazine ring in Me-COP is lower than that in COP, which indicates that the lone pair electrons on nitrogen atom are more inclined to the direction of cyclotriphosphazene due to

the hyperconjugation of methyl group. It can be seen that when the sample is in the LUMO state, the electrons have completely covered the imine bond, which is more conducive to the migration of electrons. The entire D-A structure of Ph-COP is completely destroyed due to the introduction of the phenyl group with large π -bonds, and the delocalized electrons on the whole skeleton increased significantly. ELF further confirms that the electron density on s-triazine ring in Me-COP is lower than that in COP, and the delocalized electrons on the cyclotriphosphazene are significantly increased due to the large π - π bond of benzene ring (Fig. 6a-c and S26).

DFT calculations were carried out to look into the reaction networks in accordance with the findings of the in-situ FT-IR study in order to understand the routes of photocatalytic CO₂ reduction. [53,54] Fig. 6d depicts the free energy diagram of the ideal chemical pathway for the synthesis of CO and CH₄. Where active sites the electrons travel to during the earliest stages of adsorption and activation is a crucial process. [55] According to the theoretical calculation, the lone pair electrons on the s-triazine ring (C=N) can effectively adsorb CO₂ molecules, and once CO₂ molecules are adsorbed at this active site, it is unfavourable for the continuous protonation in terms of thermodynamics (Fig. S27). [56] The CO₂ molecule can choose the lower Gibbs free energy of the cyclotriphosphazene ring (Active site 2) as the active site by adding inert groups, such as methyl groups (Fig. S28). As a result, the electrons in CO₂ move from the active site to the C 2p orbital, effectively generating *CO₂ species, which then efficiently undergoes multi-step protonation to generate CH₄. The first generation of *COOH, which is typically regarded as the rate-determining phase, is thought to be an inevitable step in the subsequent processes of CO₂ reduction. [57,58] Hence, for Me-COP, it is thermodynamically advantageous for *COOH to change into *CO, which is advantageous for its subsequent hydrogenation reduction. [59,60] According to the examination of in-situ FT-IR measurements and other reports mentioned above, *CHO is the essential intermediary for creating CH₄. [61] The hydrogenation of the *CO intermediate to produce *CHO (0.2 eV) is more advantageous thermodynamically than the desorption to produce CO (0.76 eV). In other words, the photoreduction reaction continues to lead to the creation of *CHO after producing *CO. [62] As a result, it is possible to gradually manufacture *CH₂O, *CH₂OH, and *CH₃OH from *CO, leading to the selective creation of CH₄ as the primary product.

In view of the above results, a possible reaction mechanism of selective reduction of CO₂ and selective oxidation of thioether to sulfoxide in Me-COP sample was proposed (Fig. 6e). For the reduction reaction, Me-COP generates photogenerated electrons under visible light illumination, and then the photoinduced electrons react rapidly with CO₂ molecules to selective formation of CH₄ through multi-step protonation reaction. For the oxidation reaction, Me-COP effectively produces and separates electron-hole pairs when exposed to visible light. This is followed by photoexcited electron reduction of O₂ to ¹O₂, which forms a peroxysulfonyl intermediate with the thioether, and finally CH₃CH₂OH reacts with the peroxysulfonyl intermediate to form water and methyl phenyl sulfoxide, respectively. Based on experimental data and theoretical calculations, the significant role of the methyl group, an inert group, in the D-A conjugated polymer has been demonstrated.

4. Conclusions

In summary, the introduction of inert groups into D-A conjugated polymers has constructed for two opposite photocatalytic reactions. Me-COP shows excellent photocatalytic reduction of CO₂ to CH₄ with high selectivity, and can also be used for photocatalytic selective oxidation of thioether to sulfoxide. The experimental and computational results show that the introduction of methyl group retains the D-A structure in conjugated polymer. The hyperconjugation in the methyl dispersed the nitrogen solitary electrons on the triazine ring and gave a large number of delocalized electrons to the imine bond, thus accelerating the migration of photogenerated carriers. The steric hindrance makes the adsorption of

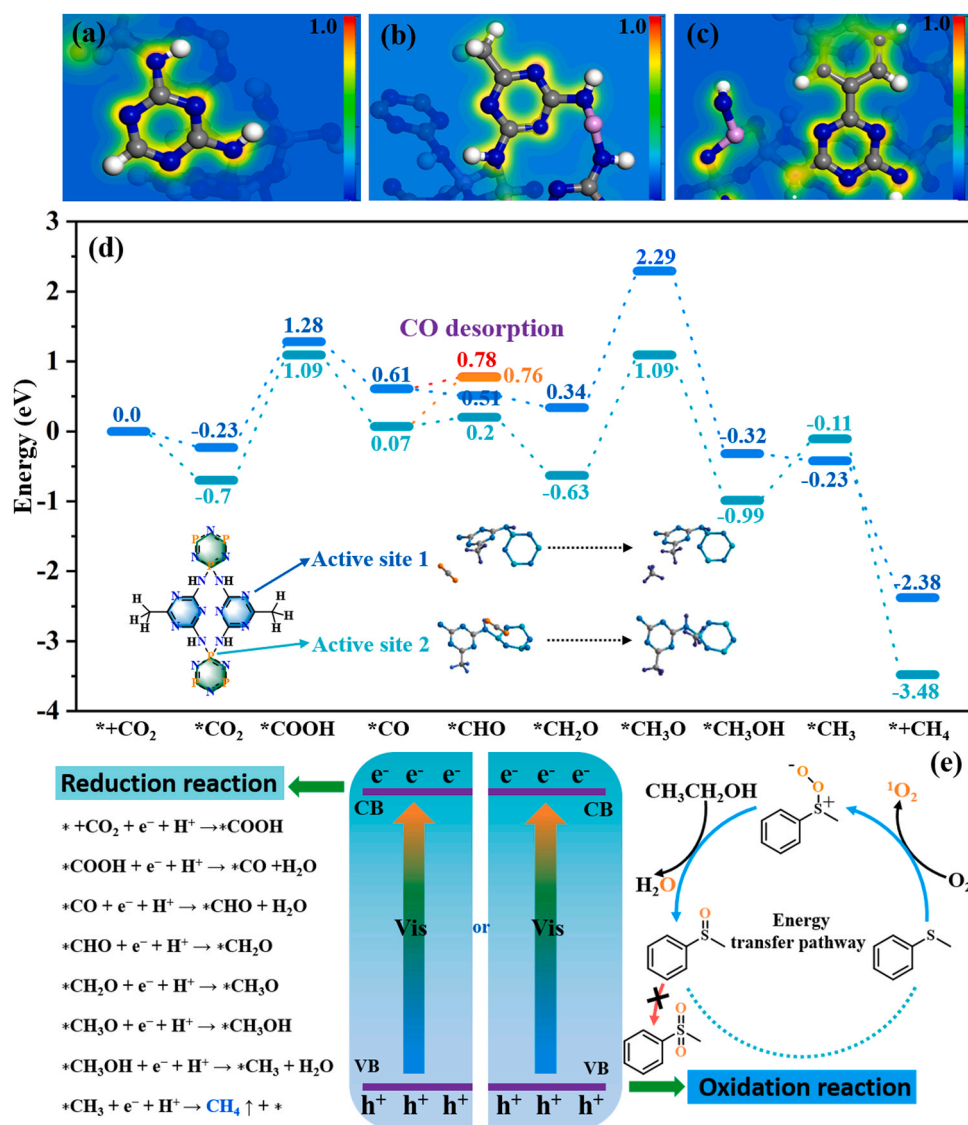


Fig. 6. The electron localization function slice diagram for (a) COP, (b) Me-COP and (c) Ph-COP samples. (d) Free energy diagrams for reduction of CO₂ to CH₄ over the Me-COP sample based on DFT calculation. (e) Possible photocatalytic mechanism of Me-COP involving different reaction intermediates.

reactants more orderly, and also shortens the distance of electron migration to reactants. A novel tactical approach to developing effective photocatalysts for both the reduction of CO₂ and the oxidation of thioethers could result from the usage of adaptable conjugated polymers with inert groups.

CRediT authorship contribution statement

Fengxuan Zhang: Conceptualization, Data curation, Formal analysis, Investigation, Methodology, Writing – original draft. **Fanxing Zhou:** Validation, Investigation, Formal analysis. **Shiheng Yin:** Investigation, Writing – review & editing. **Bei Long:** Methodology, Writing-review & editing. **Guo-Jun Deng:** Writing – review & editing, Formal analysis. **Atif Ali:** Visualization, Writing – review & editing. **Ting Song:** Writing – review & editing, Conceptualization, Investigation, Formal analysis, Visualization, Funding acquisition.

Declaration of Competing Interest

The authors declare that they have no known competing financial interests or personal relationships that could have appeared to influence

the work reported in this paper.

Data availability

Data will be made available on request.

Acknowledgements

We are extremely grateful for the financial support of General Project of Education Department of Hunan Province (21C008), Open Research Fund of School of Chemistry and Chemical Engineering, Henan Normal University (2022C02), the Hunan Provincial Natural Science Foundation of China (2021JJ40529) and the research fund of the Science and Technology Innovation Program of Hunan Province (2020RC2076).

Appendix A. Supporting information

Supplementary data associated with this article can be found in the online version at [doi:10.1016/j.apcatb.2023.123004](https://doi.org/10.1016/j.apcatb.2023.123004).

References

- [1] S. Ezendam, M. Herran, L. Nan, C. Gruber, Y. Kang, F. Gröbmeyer, R. Lin, J. Gargiulo, A.S. Castillo, E. Cortés, Hybrid plasmonic nanomaterials for hydrogen generation and carbon dioxide reduction, *ACS Energy Lett.* 7 (2022) 778–815.
- [2] S.C. Peter, Reduction of CO₂ to chemicals and fuels: a solution to global warming and energy crisis, *ACS Energy Lett.* 3 (2018) 1557–1561.
- [3] J.D. Xiao, R. Li, H.L. Jiang, Metal-organic framework-based photocatalysis for solar fuel production, *Small, Methods* 7 (2023) 2201258–2201294.
- [4] Ž. Kovačić, B. Likozar, M. Huš, Photocatalytic CO₂ reduction: a review of Ab initio mechanism, kinetics, and multiscale modeling simulations, *ACS Catal.* 10 (2020) 14984–15007.
- [5] T.R. Chen, F.S. Wu, H.P. Lee, K.H.C. Chen, Diiridium bimetallic complexes function as a redox switch to directly split carbonate into carbon monoxide and oxygen, *J. Am. Chem. Soc.* 138 (2016) 3643–3646.
- [6] H. An, Y. Hou, S. Chang, J. Zhang, Q. Zhu, Highly efficient oxidation of various thiophers catalyzed by organic ligand-modified polyoxomolybdates, *Inorg. Chem. Front.* 7 (2020) 169–176.
- [7] C. Ye, Y. Zhang, A. Ding, Y. Hu, H. Guo, Visible light sensitizer-catalyzed highly selective photo oxidation from thiophers into sulfoxides under aerobic condition, *Sci. Rep.* 8 (2018) 2205–2211.
- [8] L. Xiong, J. Tang, Strategies and challenges on selectivity of photocatalytic oxidation of organic substances, *Adv. Energy Mater.* 11 (2021) 2003216–2003235.
- [9] I. Shafiq, S. Shafique, P. Akhter, G. Abbas, A. Qurashi, M. Hussain, Efficient catalyst development for deep aerobic photocatalytic oxidative desulfurization: recent advances, confines, and outlooks, *Catal. Rev.* 64 (2022) 789–834.
- [10] B. Zhang, J. Li, B. Zhang, R. Chong, R. Li, B. Yuan, S.M. Lu, C. Li, Selective oxidation of sulfides on Pt/BiVO₄ photocatalyst under visible light irradiation using water as the oxygen source and dioxygen as the electron acceptor, *J. Catal.* 332 (2015) 95–100.
- [11] Y. Li, T.X. Luan, K. Cheng, D. Zhang, W. Fan, P.Z. Li, Y. Zhao, Effective photocatalytic initiation of reactive oxygen species by a photoactive covalent organic framework for oxidation reactions, *ACS Mater. Lett.* 4 (2022) 1160–1167.
- [12] S. Ma, T. Deng, Z. Li, Z. Zhang, J. Jia, Q. Li, G. Wu, H. Xia, S.W. Yang, X. Liu, Photocatalytic hydrogen production on a sp²-carbon-linked covalent organic framework, *Angew. Chem. Int. Ed.* 61 (2022) e202208919–202208927.
- [13] J. Sun, H.S. Jena, C. Krishnaraj, K.S. Rawat, S. Abednatanzi, J. Chakraborty, A. Laemont, W. Liu, H. Chen, Y.Y. Liu, K. Leus, H. Vrielinck, V.V. Speybroeck, P. Voort, Pyrene-based covalent organic frameworks for photocatalytic hydrogen peroxide production, *Angew. Chem. Int. Ed.* (2023) e202216719–e202216729.
- [14] S. Li, M.F. Wu, T. Guo, L.L. Zheng, D. Wang, Y. Mu, Q.J. Xing, J.P. Zou, Chlorine-mediated photocatalytic hydrogen production based on triazine covalent organic framework, *Appl. Catal. B Environ.* 272 (2020) 118989–118998.
- [15] M. Wu, Z. Shan, J. Wang, T. Liu, G. Zhang, Three-dimensional covalent organic framework with tty topology for enhanced photocatalytic hydrogen peroxide production, *Chem. Eng. J.* 454 (2023) 140121–140128.
- [16] A. Savateev, Y. Markushyna, C.M. Schüßlbauer, T. Ullrich, D.M. Guldi, M. Antonietti, Unconventional photocatalysis in conductive polymers: reversible modulation of PEDOT: PSS conductivity by long-lived poly(heptazine imide) radicals, *Angew. Chem. Int. Ed.* 60 (2021) 7436–7443.
- [17] Y. Fang, X. Fu, X. Wang, Diverse polymeric carbon nitride-based semiconductors for photocatalysis and variations, *ACS Mater. Lett.* 2 (2020) 975–980.
- [18] A. Hayat, N. Shaishta, S.K.B. Mane, A. Hayat, J. Khan, A.U. Rehman, T. Li, Molecular engineering of polymeric carbon nitride based donor-acceptor conjugated copolymers for enhanced photocatalytic full water splitting, *J. Colloid Interface Sci.* 560 (2020) 743–754.
- [19] Y. Bai, X. Yi, B. Li, S. Chen, Z. Fan, Constructing porous polyimide/carbon quantum dots aerogel with efficient photocatalytic property under visible light, *Appl. Surf. Sci.* 578 (2022) 151993–152002.
- [20] B. Xu, S. Wei, Y. Liu, S. Zhao, L. Qian, Preparation of an organometallic complex based on phosphonitrile and its flame retardant application in epoxy resin, *J. Mater. Res. Technol.* 21 (2022) 4921–4939.
- [21] S. Guo, H. Zhang, Y. Chen, Z. Liu, B. Yu, Y. Zhao, Z. Yang, B. Han, Z. Liu, Visible-light-driven photoreduction of CO₂ to CH₄ over N,O,P-containing covalent organic polymer submicrospheres, *ACS Catal.* 8 (2018) 4576–4581.
- [22] B. Chen, M. Dong, S. Liu, Z. Xie, J. Yang, S. Li, Y. Wang, J. Du, H. Liu, B. Han, CO₂ hydrogenation to formate catalyzed by Ru coordinated with a N,P-containing polymer, *ACS Catal.* 10 (2020) 8557–8566.
- [23] V.S. Kale, M. Hwang, H. Chang, J. Kang, S.I. Chae, Y. Jeon, J. Yang, J. Kim, Y.J. Ko, Y. Piao, T. Hyeon, Microporosity-controlled synthesis of heteroatom codoped carbon nanocages by wrap-bake-sublime approach for flexible all-solid-state-supercapacitors, *Adv. Funct. Mater.* 28 (2018) 1803786–1803798.
- [24] F. Hu, H. Wang, Y. Zhang, X. Shen, G. Zhang, Y. Pan, J.T. Miller, K. Wang, S. Zhu, X. Yang, C. Wang, X. Wu, Y. Xiong, Z. Peng, Designing highly efficient and long-term durable electrocatalyst for oxygen evolution by coupling B and P into amorphous porous NiFe-based material, *Small* 15 (2019) 1901020–1901030.
- [25] X. Liu, F. Liu, J. Yu, G. Xiong, L. Zhao, Y. Sang, S. Zuo, J. Zhang, H. Liu, W. Zhou, Charge redistribution caused by S,P synergistically active Ru endows an ultrahigh hydrogen evolution activity of S-doped RuP embedded in N,P,S-doped carbon, *Adv. Sci.* 7 (2020) 2001526–2001534.
- [26] G. Zou, H. Hou, C.W. Foster, C.E. Banks, T. Guo, Y. Jiang, Y. Zhang, X. Ji, Advanced hierarchical vesicular carbon Co-doped with S, P, N for high-rate sodium storage, *Adv. Sci.* 5 (2018) 1800241–1800250.
- [27] D.W. Stephan, Frustrated lewis pairs, *J. Am. Chem. Soc.* 137 (2015) 10018–10032.
- [28] D.W. Stephan, G. Erker, Frustrated lewis pair chemistry: development and perspectives, *Angew. Chem. Int. Ed.* 54 (2015) 6400–6441.
- [29] T. Li, J. Shi, Z. Liu, W. Xie, K. Cui, B. Hu, G. Che, L. Wang, T. Zhou, C. Liu, Constructing porous intramolecular donor-acceptor integrated carbon nitride doped with m-aminophenol for boosting photocatalytic degradation and hydrogen evolution activity, *Catal. Sci. Technol.* 12 (2022) 4591–4604.
- [30] Z. Li, H. Fang, Z. Chen, W. Zou, C. Zhao, X. Yang, Regulating donor-acceptor interactions in triazine-based conjugated polymers for boosted photocatalytic hydrogen production, *Appl. Catal. B Environ.* 312 (2022) 121374–121383.
- [31] L. Yuan, Y.Y. Zou, L. Zhao, C.Q. Zhang, J. Wang, C. Liu, G.F. Wei, C.Z. Yu, Unveiling the lattice distortion and electron-donating effects in methoxy-functionalized MOF photocatalysts for H₂O₂ production, *Appl. Catal. B Environ.* 318 (2022) 121859–121868.
- [32] C.M. Boudreaux, N.P. Liyanage, H. Shirley, S. Siek, D.L. Gerlach, F. Qu, J. H. Delcamp, E.T. Papish, Ruthenium(II) complexes of pyridinol and N-heterocyclic carbene derived pincers as robust catalysts for selective carbon dioxide reduction, *Chem. Commun.* 53 (2017) 11217–11220.
- [33] H. Chen, H.S. Jena, X. Feng, K. Leus, P. Voort, Engineering covalent organic frameworks as heterogeneous photocatalysts for organic transformations, *Angew. Chem. Int. Ed.* 61 (2022) e202204938–e202204963.
- [34] M.W. Logan, S. Ayad, J.D. Adamson, T. Dilbeck, K. Hanson, F.J. Romo, Systematic variation of the optical bandgap in titanium based isorecticular metal-organic frameworks for photocatalytic reduction of CO₂ blue light, *J. Mater. Chem. A* 5 (2017) 11854–11863.
- [35] K. Chen, Y. Liu, Y. Hu, M. Yuan, X. Zheng, X. Huang, Facile synthesis of amino-functionalized polyphosphazene microspheres and their application for highly sensitive fluorescence detection of Fe³⁺, *J. Appl. Polym. Sci.* 137 (2020) 48937–48945.
- [36] J. Yin, T. Zhang, E. Schulman, D. Liu, J. Meng, Hierarchical porous metallized poly-melamine-formaldehyde (PMF) as a low-cost and high-efficiency catalyst for cyclic carbonate synthesis from CO₂ and epoxides, *J. Mater. Chem. A* 6 (2018) 8441–8448.
- [37] C. Han, S. Xiang, M. Ge, P. Xie, C. Zhang, J.X. Jiang, An efficient electron donor for conjugated microporous polymer photocatalysts with high photocatalytic hydrogen evolution activity, *Small* 18 (2022) 2202072–2202081.
- [38] F. Yu, Z. Zhu, C. Li, W. Li, R. Liang, S. Yu, Z. Xu, F. Song, Q. Ren, Z. Zhang, A redox-active perylene-anthraquinone donor-acceptor conjugated microporous polymer with an unusual electron delocalization channel for photocatalytic reduction of uranium (VI) in strongly acidic solution, *Appl. Catal. B Environ.* 314 (2022) 121467–121478.
- [39] Z. Zhu, H. Huang, L. Liu, F. Chen, N. Tian, Y. Zhang, H. Yu, Chemically bonded α-Fe₂O₃/Bi₄Mo₈Cl dot-on-plate Z-scheme junction with strong internal electric field for selective photo-oxidation of aromatic alcohols, *Angew. Chem. Int. Ed.* 61 (2022) e202203519–e202203528.
- [40] J. Jiang, X. Wang, Q. Xu, Z. Mei, L. Duan, H. Guo, Understanding dual-vacancy heterojunction for boosting photocatalytic CO₂ reduction with highly selective conversion to CH₄, *Appl. Catal. B Environ.* 316 (2022) 121679–121690.
- [41] K. Song, S. Liang, X. Zhong, M. Wang, X. Mo, X. Lei, Z. Lin, Tailoring the crystal forms of the Ni-MOF catalysts for enhanced photocatalytic CO₂-to-CO performance, *Appl. Catal. B Environ.* 309 (2022) 121232–121240.
- [42] J. Deng, K.B. Tayeb, C. Dong, P. Simon, M. Marinova, M. Dubois, J.C. Morin, W. Zhou, M. Capron, V.V. Ordonsky, TEMPO-Ru-BEA composite material for the selective oxidation of alcohols to aldehydes, *ACS Catal.* 12 (2022) 8925–8935.
- [43] X. Yan, L. Wang, X. Tan, B. Tian, J. Zhang, Surface-enhanced raman spectroscopy assisted by radical capturer for tracking of plasmon-driven redox reaction, *Sci. Rep.* 6 (2016) 30193–30200.
- [44] J. Gu, Y. Yu, S. Chen, W. Shi, Y. Wang, Y. Liao, H. Chen, F. Jiang, Heterojunction photocatalyst of cavity shaped Bi₂S₃/g-C₃N₄ for bisphenol A degradation: regulation of internal electric field via assistance of interfacial functional groups, *Chem. Eng. J.* 424 (2021) 130539–130552.
- [45] Q. Li, X. Lan, G. An, L.R. Sandoval, Z. Wang, G. Bai, Visible-light-responsive anthraquinone functionalized covalent organic frameworks for metal-free selective oxidation of sulfides: effects of morphology and structure, *ACS Catal.* 10 (2020) 6664–6675.
- [46] J.L. Shi, X. Lang, Assembling polydopamine on TiO₂ for visible light photocatalytic selective oxidation of sulfides with aerial O₂, *Chem. Eng. J.* 392 (2020) 123632–123644.
- [47] Y. Qian, H. Wang, X. Li, T. Song, Y. Pei, L. Liu, B. Long, X. Wu, X. Wang, Sn-doped BiOCl nanosheet with synergistic H⁺/Zn²⁺ co-insertion for “rocking chair” zinc-ion battery, *J. Energy Chem.* 81 (2023) 623–632.
- [48] W. Dai, P. Wang, J. Long, Y. Xu, M. Zhang, L. Yang, J. Zou, X. Luo, S. Luo, Constructing robust Bi active sites in situ on α-Bi₂O₃ for efficient and selective photoreduction of CO₂ to CH₄ via directional transfer of electrons, *ACS Catal.* 13 (2023) 2513–2522.
- [49] M. Wang, M. Shen, X. Jin, J. Tian, M. Li, Y. Zhou, L. Zhang, Y. Li, J. Shi, Oxygen vacancy generation and stabilization in CeO_{2-x} by Cu introduction with improved CO₂ photocatalytic reduction activity, *ACS Catal.* 9 (2019) 4573–4581.
- [50] J. Wu, X. Li, W. Shi, P. Ling, Y. Sun, X. Jiao, S. Gao, L. Liang, J. Xu, W. Yan, C. Wang, Y. Xie, Efficient visible-light-driven CO₂ reduction mediated by defect-engineered BiOBr atomic layers, *Angew. Chem. Int. Ed.* 57 (2018) 8719–8723.
- [51] Z. Ma, P. Li, L. Ye, Y. Zhou, F. Su, C. Ding, H. Xie, Y. Bai, P.K. Wong, Oxygen vacancies induced exciton dissociation of flexible BiOCl nanosheets for effective photocatalytic CO₂ conversion, *J. Mater. Chem. A* 5 (2017) 24995–25004.
- [52] T. Geng, C. Zhang, M. Liu, C. Hu, G. Chen, Preparation of biimidazole-based porous organic polymers for ultrahigh iodine capture and formation of liquid complexes with iodide/polyiodide ions, *J. Mater. Chem. A* 8 (2020) 2820–2826.

- [53] J. Zhou, J. Li, L. Kan, L. Zhang, Q. Huang, Y. Yan, Y. Chen, J. Liu, S.L. Li, Y.Q. Lan, Linking oxidative and reductive clusters to prepare crystalline porous catalysts for photocatalytic CO₂ reduction with H₂O, *Nat. Commun.* 13 (2022) 4681–4691.
- [54] S. Barman, A. Singh, F.A. Rahimi, T.K. Maji, Metal-free catalysis: a redox-active donor–acceptor conjugated microporous polymer for selective visible-light-driven CO₂ reduction to CH₄, *J. Am. Chem. Soc.* 143 (2021) 16284–16292.
- [55] H.B. Yang, S.F. Hung, S. Liu, K. Yuan, S. Miao, L. Zhang, X. Huang, H.Y. Wang, W. Cai, R. Chen, J. Gao, X. Yang, W. Chen, Y. Huang, H.M. Chen, C.M. Li, T. Zhang, B. Liu, Atomically dispersed Ni(I) as the active site for electrochemical CO₂ reduction, *Nat. Energy* 3 (2018) 140–147.
- [56] Z. Chen, M.R. Gao, Y.Q. Zhang, N. Duan, T. Fan, J. Xiao, J. Zhang, Y. Dong, J. Li, X. Yi, J.L. Luo, Tuning local carbon active sites saturability of graphitic carbon nitride to boost CO₂ electroreduction towards CH₄, *Nano Energy* 73 (2020) 104833–104843.
- [57] Y.Y. Birdja, E.P. Gallent, M.C. Figueiredo, A.J. Göttele, F.C. Vallejo, M.T.M. Koper, Advances and challenges in understanding the electrocatalytic conversion of carbon dioxide to fuels, *Nat. Energy* 4 (2019) 732–745.
- [58] D. Gao, R.M. Ais, H.S. Jeon, B.R. Cuenya, Rational catalyst and electrolyte design for CO₂ electroreduction towards multicarbon products, *Nat. Catal.* 2 (2019) 198–210.
- [59] Z. Wu, H. Wu, W. Cai, Z. Wen, B. Jia, L. Wang, W. Jin, T. Ma, Engineering bismuth-tin interface in bimetallic aerogel with a 3D porous structure for highly selective electrocatalytic CO₂ reduction to HCOOH, *Angew. Chem. Int. Ed.* 60 (2021) 12554–12559.
- [60] C. Zhang, S. Yang, J. Wu, M. Liu, S. Yazdi, M. Ren, J. Sha, J. Zhong, K. Nie, A. S. Jalilov, Z. Li, H. Li, B.I. Yakobson, Q. Wu, E. Ringe, H. Xu, P.M. Ajayan, J. M. Tour, Electrochemical CO₂ reduction with atomic iron-dispersed on nitrogen-doped graphene, *Adv. Energy Mater.* 8 (2018) 1703487–1703496.
- [61] M. Ma, B.J. Jin, P. Li, M.S. Jung, J.I. Kim, Y. Cho, S. Kim, J.H. Moon, J.H. Park, Ultrahigh electrocatalytic conversion of methane at room temperature, *Adv. Sci.* 4 (2017) 1700379–1700388.
- [62] P. Liu, Z. Huang, X. Gao, X. Hong, J. Zhu, G. Wang, Y. Wu, J. Zeng, X. Zheng, Synergy between palladium single atoms and nanoparticles via hydrogen spillover for enhancing CO₂ photoreduction to CH₄, *Adv. Mater.* 34 (2022) 2200057–2200068.